

Substantial Risk of 21st Century AMOC Tipping even under Moderate Climate Change

René M. van Westen^{1*}, Elian Y.P. Vanderborght¹,
Michael Kliphuis¹, Henk A. Dijkstra¹

¹Department of Physics, Institute for Marine and Atmospheric research
Utrecht, Utrecht University, Princetonplein 5, Utrecht, 3584 CC, the
Netherlands.

*Corresponding author(s). E-mail(s): r.m.vanwesten@uu.nl;
Contributing authors: e.y.p.vanderborght@uu.nl; m.kliphuis@uu.nl;
h.a.dijkstra@uu.nl;

Abstract

The Atlantic Meridional Overturning Circulation (AMOC) is a key component of the climate system and considered to be a tipping element. There is still a large uncertainty on the critical global warming level at which the AMOC will start to collapse. Here we analyse targeted climate model simulations, together with observations, reanalysis products and a suite of state-of-the-art climate model results to reassess this critical global warming level. We find a critical threshold of +3°C global mean surface temperature increase compared to pre-industrial with a lower bound of +2.2°C (10%-CI). Such global mean surface temperature anomalies are expected to be reached after 2050. This means that the AMOC is more likely than not ($\geq 50\%$) to tip within the 21st century under a middle-of-the-road climate change scenario and very likely ($\geq 90\%$) to tip under a high emissions scenario. The AMOC collapse induced cooling is shown to be offset by the regional warming over Northwestern Europe during the 21st century, but will still induce severe impacts on society.

Keywords: AMOC collapse, Climate change, Climate impacts

Main

The Atlantic Meridional Overturning Circulation (AMOC) has been identified as a tipping element in the climate system [1, 2]. The AMOC transports heat and salt through the global ocean [3], and strong reductions in its strength severely impact climate over large parts of the world [4–6]. Given these potentially severe global consequences, it is not surprising that the present-day AMOC is closely monitored along several arrays [7–9] in the Atlantic Ocean.

The 20-year long observational AMOC strength time series from the RAPID-MOCHA array at 26°N [8] has been complemented by sea surface temperature (SST)-based reconstructions [10–14]. These AMOC reconstructions indicate a gradual weakening of the AMOC by a few Sverdrups ($1 \text{ Sv} = 10^6 \text{ m}^3\text{s}^{-1}$) since 1900 and also suggest that the AMOC is approaching its tipping point [15, 16]. However, they may not adequately capture the AMOC behaviour and are prone to false positive signals [6, 17].

AMOC strength projections from the Coupled Model Intercomparison Project (CMIP) phase 6 (CMIP6) do not show evidence of a 21st century AMOC collapse, and their projections appear quite insensitive with respect to the greenhouse gas emission scenario used [18]. The sixth Intergovernmental Panel on Climate Change (IPCC) report states with *medium confidence* that an AMOC collapse will not occur during the 21st century [19]. Moreover, an analysis of critical global warming levels of tipping elements [2] finds that the AMOC is *likely* to tip only above +4°C global mean surface temperature increase with respect to the pre-industrial level. This suggests a relatively stable AMOC, even under high greenhouse gas emission scenarios such as the Shared Socioeconomic Pathway (SSP) 3-7.0.

Recently, a quasi-equilibrium hosing simulation [6] with the Community Earth System Model (CESM) showed that the pre-industrial AMOC collapses under the imposed freshwater flux forcing. While this simulation was still idealised as no climate change forcing was included, it provides the basis for developing efficient diagnostics for an AMOC collapse under transient 21st century forcing. Here, we conduct additional targeted CESM simulations of the 21st century AMOC under climate change and compare the results with those of 24 CMIP6 models, with the aim to reassess the critical global warming level at which the AMOC starts to collapse.

AMOC Collapse in the Pre-industrial CESM

The quasi-equilibrium hosing simulation (see Methods, [6]) was conducted under constant pre-industrial radiative forcing conditions. The AMOC strength is plotted in Figure 1a versus the freshwater flux forcing (F_H) which linearly increases from 0 to 0.66 Sv over 2,200 model years; the AMOC collapses at about 0.525 Sv (model year 1,758 [6]). From this simulation the dominant physical mechanisms of AMOC tipping can be quantified and used to analyse model simulations under climate change.

Before the collapse (Figure S1), the AMOC decline is linked to potential density changes over the northern isopycnal outcropping region (located at 40°N – 60°N, Figure S1c). The AMOC over the isopycnal outcropping region is in thermal wind balance with the meridional density gradient over this region [20, 21]. The upper

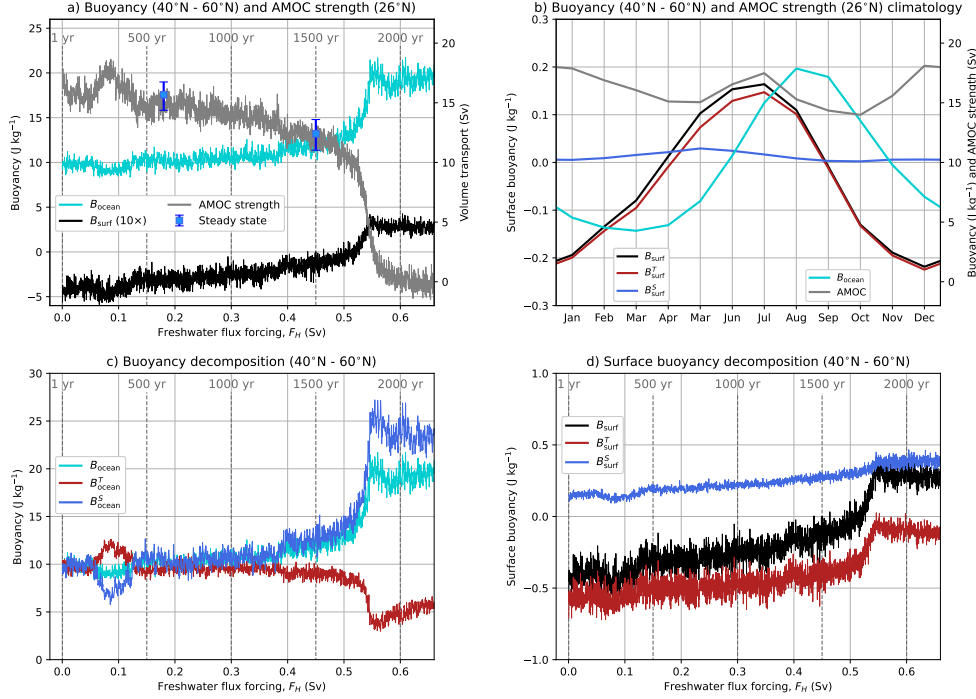


Fig. 1 Buoyancy and AMOC responses under the hosing. (a): The AMOC strength at 1,000 m and 26°N (yearly averages) under the quasi-equilibrium hosing and for the two statistical steady states at constant forcing $F_H = 0.18$ Sv and $F_H = 0.45$ Sv. The upper 1,000 m buoyancy (B_{ocean} , yearly averages) and surface buoyancy (B_{surf} , yearly sums), spatially averaged over the North Atlantic Ocean (40°N – 60°N). (b): Mean seasonal cycle over the first 50 model years for the quantities plotted in panel a. (c): The upper 1,000 m buoyancy B_{ocean} (yearly averages), decomposition for the temperature (B_{ocean}^T) and salinity (B_{ocean}^S). (d): The surface buoyancy B_{surf} (yearly sums) decomposition for the heat fluxes (B_{surf}^T) and freshwater fluxes (B_{surf}^S).

1,000 m potential density changes over the isopycnal outcropping region primarily drive the AMOC decline and we quantify these changes by determining the upper ocean buoyancy (B_{ocean} , see Methods) over the region. The quantity B_{ocean} has indeed the opposite response to that of the AMOC strength under the quasi-equilibrium hosing (Figure 1a).

The outcropping of isopycnals at 40°N – 60°N is governed by surface winds, interior mixing and loss of surface buoyancy (B_{surf}) [20]. Interior ocean isopycnals only surface when B_{surf} remains net negative over time scales longer than one year. There is a strong seasonal cycle in both B_{ocean} and B_{surf} , where the surface buoyancy leads by about 2 months (Figure 1b). The surface buoyancy is primarily driven by atmosphere-ocean heat fluxes and the relatively large negative winter values cause strong vertical mixing (i.e., deep convection) over the isopycnal outcropping region. Once B_{surf} switches sign, there is no outcropping of isopycnals and only a weak and diffusive AMOC can exist [22]. The quantity B_{surf} is linked to water mass transformation and hence AMOC

strength [23, 24] and indeed B_{surf} and AMOC strength have the opposite response under the hosing (Figure 1a).

From the temperature and salinity buoyancy decompositions of B_{ocean} (B_{ocean}^T and B_{ocean}^S , respectively, see Methods) it is found that salinity perturbations weaken the AMOC under the hosing (Figure 1c). The non-linear increase in B_{ocean}^S after 1350 years ($F_H > 0.4$ Sv) indicates a positive salt-advection feedback. This feedback is destabilising the AMOC as salinity anomalies are amplified through their effect on the AMOC strength and pattern [25, 26]. The AMOC weakening and associated reduced meridional heat transport result in lower SSTs (i.e., the characteristic AMOC fingerprint [10]) and induce ocean buoyancy loss which stabilises the AMOC. The B_{ocean}^T responses have a passive and opposite role to the B_{ocean}^S responses.

The quantity B_{surf} is decomposed in a similar way (Figure 1d) and the B_{surf}^S increase is primarily driven by the freshwater flux forcing. Changes in AMOC strength, driven by freshening of the isopycnal outcropping region, reduce the surface ocean and atmosphere temperatures. These ocean-atmosphere temperature differences modify the heat fluxes (Figure S2) and show that lower SSTs effectively lose less heat to the atmosphere and reduce the magnitude of B_{surf}^T . It should be noted that the lower temperatures enhance sea-ice formation conditions around Greenland ($> 60^\circ\text{N}$) and, via advection of sea ice, increase the sea-ice area over the isopycnal outcropping region. The expanding sea-ice pack enhances the albedo and strongly reduces the ocean-atmosphere fluxes [27]. The bottom line is that the freshwater flux forcing increases B_{surf}^S and, through complex AMOC feedbacks, leads to an equally important contribution in B_{surf}^T . For example, B_{surf} increased by 0.28 J kg^{-1} for $F_H = 0.45$ Sv (model years 1476 – 1525) compared to beginning of the simulation, where B_{surf}^S contributed 47% and B_{surf}^T contributed 53%.

The isopycnal outcropping region changes from losing surface buoyancy to gaining surface buoyancy around the AMOC tipping event ($F_H = 0.525$ Sv, model year 1750). Thereafter the region is gaining net buoyancy through its surface. The collapse is caused by the destabilising salt-advection feedback and a positive B_{surf} ensures that a collapsed state will be reached. What is, however, most important from these results is that the buoyancy diagnostics considered can be used to analyse AMOC behaviour in model simulations under climate change forcing.

The AMOC Collapse under Climate Change

From the quasi-equilibrium hosing we branched off 500-year long simulations under constant freshwater flux forcing to find statistical equilibria for $F_H = 0.18$ Sv and $F_H = 0.45$ Sv (Figure 1a, with more details in [28]). The simulation with the higher freshwater flux forcing is closer to the AMOC tipping point under constant pre-industrial radiative forcing conditions. From the end of the statistical equilibria, we branched off the historical forcing (1850 – 2005) followed by the Representative Concentration Pathway (RCP) 4.5 and 8.5 scenarios (2006 – 2100) while keeping the value of F_H fixed for each simulation. Finally, after the year 2100, we kept the forcing conditions fixed at their 2100 forcing levels and ran the simulations for an additional 400 years (up to 2500) to find the statistical equilibria under these future forcing

conditions. Ice sheet dynamics are important on such long timescales, but ice sheets are prescribed in the CESM simulations. Hence the long-term results only represent equilibria under a substantially changed radiative forcing, but with present-day ice sheets.

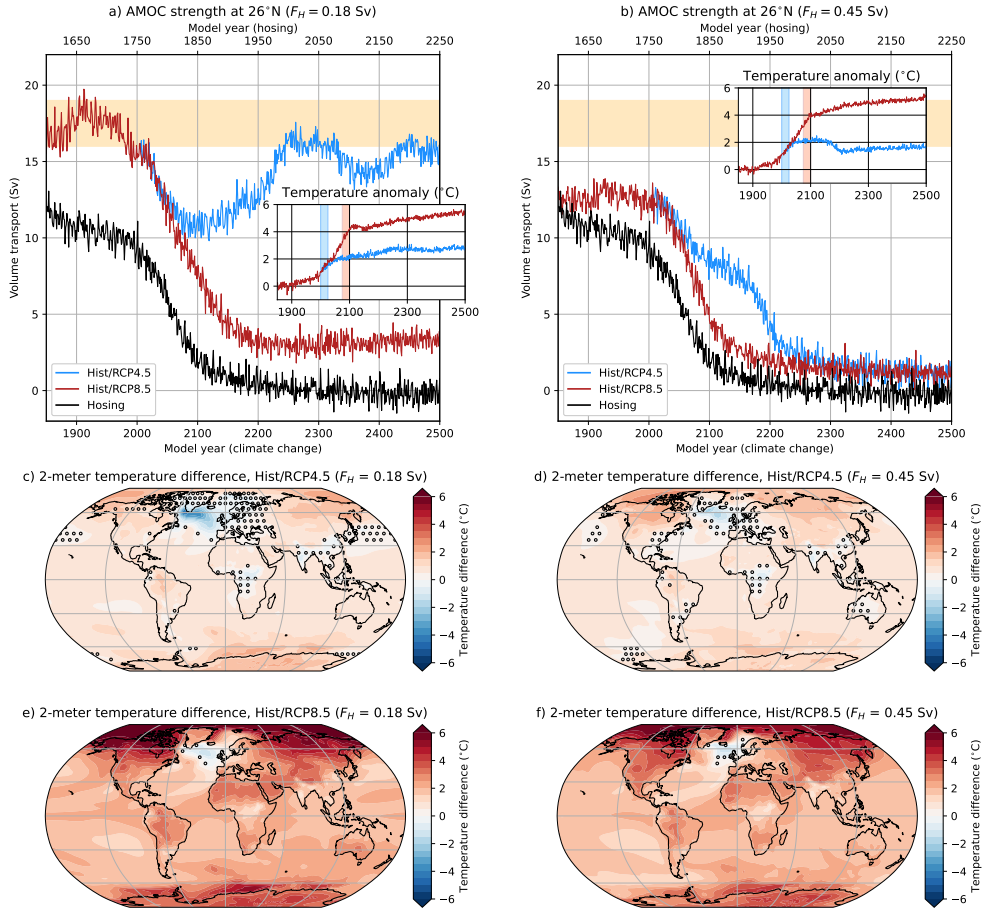


Fig. 2 The AMOC responses under climate change. The AMOC strength at 1,000 m and 26°N under the two climate change scenarios (Hist/RCP4.5 and Hist/RCP8.5) and for (a): $F_H = 0.18$ Sv and (b): $F_H = 0.45$ Sv. For reference, the AMOC collapse under the hosing is also shown and is centred around the AMOC tipping event (black curve, top x-axis). The yellow shading indicates the observed AMOC strength [13, 29]. The insets show the 2-meter global mean surface temperature anomaly compared to the pre-industrial period (1850 – 1899). The yearly-averaged surface temperature differences are determined between the red (2075 – 2100) and blue (2000 – 2025) shaded periods and are presented in panels c – f. The markers in panels c – f indicate non-significant ($p \geq 0.05$, two-sided Welch's t-test) differences.

The AMOC strengths at 1,000 m and 26°N under the two climate change scenarios are shown for the $F_H = 0.18$ and $F_H = 0.45$ cases in Figures 2a,b, including the global

mean surface temperature anomaly (see insets). For $F_H = 0.18$ Sv, the AMOC has a reasonable strength over the historical period compared to present-day observations (Figures 2a) but its freshwater transport at 34°S (indicated by F_{ovS}) is biased positive (Figure S3). On the other hand, for $F_H = 0.45$ Sv, the freshwater transport at 34°S is in the range of observations (Figure S3) but the historical AMOC strength is weaker than in observations (Figures 2b). The quantity F_{ovS} is an important indicator in AMOC tipping dynamics [5, 30–33] and a negative F_{ovS} sign indicates that the AMOC is closer to its tipping point under the quasi-equilibrium hosing [6].

Up to 2020, the AMOC strength remains remarkably constant for the simulations under climate change. Thereafter, the AMOC strength substantially weakens by 5 – 6 Sv under Hist/RCP4.5 and 8 – 9 Sv under Hist/RCP8.5 over the 21st century. The AMOC weakening rates under Hist/RCP8.5 are comparable to that of the hosing with a decline of 8 Sv over about 100 years (Figures 1a). The RCP4.5 and RCP8.5 scenarios show little differences in their AMOC responses up to 2050 and this is consistent with the results for the CMIP6 models [18].

The climate change scenarios for $F_H = 0.45$ Sv both show AMOC collapses and their AMOC strengths reduce to 1 Sv at the end of the simulations. The AMOC strength in RCP4.5 ($F_H = 0.45$ Sv) reduces by 3.9 Sv (-31%) in 2090 – 2100 (with respect to 1850 – 1899) and eventually collapses after 2150. This suggests that, under this scenario, an AMOC tipping event occurs somewhere in the 21st century. For $F_H = 0.18$ Sv, only the AMOC under RCP8.5 collapses and appears to stabilise around 3.5 Sv at the end of the simulation. In the RCP4.5 (and $F_H = 0.18$ Sv) scenario the AMOC weakens by 6.1 Sv (-36%) in 2090 – 2100 (with respect to 1850 – 1899) and eventually recovers to 15.7 Sv (-6.7%) at the end of the simulation. This shows that quantifying an AMOC collapse based on absolute AMOC anomalies or fractional changes [34] may misinterpret an imminent collapse.

The extended simulations provide insight into the equilibria resulting under fixed future climate forcing. Under RCP8.5 and for $F_H = 0.18$ Sv, the AMOC reduces to a weak and shallow (< 1000 m) overturning cell and the quantity F_{ovS} becomes negative (Figure S3). This is a typical characteristic of an ‘AMOC weak’ state which is an additional statistical equilibrium in the full hysteresis hosing simulation under pre-industrial conditions [5, 28]. The AMOC states resulting at $F_H = 0.45$ Sv have no clear overturning cell and their F_{ovS} values become positive. These AMOC characteristics link to an ‘AMOC off’ state as found under pre-industrial conditions as a statistical equilibrium [28].

When comparing the two RCP4.5 simulations, the temperature responses over the 21st century (Figures 2c,d) are, however, very similar. The same holds for the two RCP8.5 simulations over the 21st century (Figures 2e,f). The AMOC weakening can (partly) offset the regional warming over Northwestern Europe resulting in below-averaged surface temperature rise for a few European cities in the 21st century (Figures S4a–d). The surface temperature anomalies at the end of the simulation (i.e., the equilibrium temperatures, model years 2450 – 2499, Figure S4e–h) clearly show the strong AMOC-induced cooling when the AMOC has collapsed and are most pronounced for $F_H = 0.45$ Sv and the RCP4.5 scenario.

The Buoyancy Responses under Climate Change

Also under climate change, the B_{ocean} over the isopycnal outcropping region is related to the AMOC strength (Figures S5a–d). The B_{surf} is significantly ($p < 0.05$, [35]) increasing during the 21st century and the changes are smaller in the Hist/RCP4.5 (0.29 J kg⁻¹ and 0.26 J kg⁻¹) than in the Hist/RCP8.5 (0.49 J kg⁻¹ and 0.44 J kg⁻¹, for $F_H = 0.18$ Sv and $F_H = 0.45$ Sv, respectively). As expected, the larger increase in B_{surf} under Hist/RCP8.5 (compared to Hist/RCP4.5) can be attributed to a larger radiative forcing (Figures S5a–d). The ocean buoyancy decomposition into its temperature and salinity contributions (Figures S5e–l) clearly shows that temperature responses are forcing the AMOC. Prior to the AMOC decline of model year 2020, the temperature is weakening the AMOC by buoyancy gain (B_{ocean}^T) and thereafter salinity responses (B_{ocean}^S) start to dominate. This strong increase in B_{ocean}^S indicates a destabilising salt-advection feedback.

The buoyancy responses under climate change are clearly different from those of the quasi-equilibrium hosing simulation, because in the latter case the ocean salinity responses (B_{ocean}^S) are entirely responsible for destabilising the AMOC. Another difference is that under climate change the surface buoyancy increase is induced by heat flux (B_{surf}^T) changes and the freshwater flux (B_{surf}^S) changes have a negligible contribution. However, once the AMOC starts to decline, we find comparable (with respect to the quasi-equilibrium case) responses in the latent, sensible, longwave, evaporation and precipitation contributions (Figure S6). The AMOC sea-ice feedbacks are only relevant for the Hist/RCP4.5 and the $F_H = 0.45$ Sv case as the sea ice vastly extends under its AMOC collapse. For the other simulations, the higher background temperatures melt almost all sea ice and hence are limiting the destabilising sea-ice buoyancy contribution.

The AMOC collapses under the two RCP8.5 scenarios and the dynamics driving the collapse shares similarities to that of the hosing simulation (Figure S5). The B_{surf} increase levels off when the climate forcing becomes constant in both RCP4.5 simulations. Depending on the freshwater flux forcing, this results in either a negative B_{surf} or positive B_{surf} in 2100 for $F_H = 0.18$ Sv and $F_H = 0.45$ Sv, respectively. The AMOC eventually recovers for $F_H = 0.18$ Sv (Figure 2a), but for $F_H = 0.45$ Sv the isopycnal outcropping region slowly gains buoyancy between model years 2080 to 2150. This results in an AMOC decline of only 1 Sv between 2100 and 2150 and thereafter it fully collapses. During the AMOC collapse, B_{surf} further increases which is similar to the hosing and RCP8.5 simulations. A net negative surface buoyancy is crucial for AMOC stability [20–24] and an AMOC collapse is inevitable when B_{surf} becomes positive.

Surface Buoyancy Responses in CMIP6 models

As the B_{surf} over the isopycnal outcropping region is a diagnostic of an imminent AMOC collapse, we have determined it for 24 different CMIP6 models under the historical forcing (1850 – 2014) followed by the SSP2-4.5 and SSP5-8.5 (2015 – 2100) scenarios. In CMIP6 there are no indications for an AMOC collapse by the year 2100 [18, 36]. This is not very surprising as the typical AMOC collapse timescale is longer

than 100 years and only (substantial) AMOC weakening can be expected by 2100 (Figures 2a,b).

The behaviour of B_{surf} in CMIP6 models is similar to that in the CESM simulations discussed above and the heat fluxes primarily drive the increase over the 21st century (Figures 3a,b). The CMIP6 multi-model mean B_{surf} trends (2000 – 2100) are 0.25 (0.15 – 0.37, 10% – 90%-CI) J kg^{-1} per century and 0.37 (0.22 – 0.54, 10% – 90%-CI) J kg^{-1} per century for Hist/SSP2-4.5 and Hist/SSP5-8.5, respectively (Figure 3c and Table S1). The multi-model mean B_{surf} switches sign by 2043 and by 2036 with an associated global warming of $+1.96^\circ\text{C}$ ($+1.52^\circ\text{C}$ to $+2.37^\circ\text{C}$, 10% – 90%-CI, years 2038 – 2048) and $+1.88^\circ\text{C}$ ($+1.41^\circ\text{C}$ to $+2.31^\circ\text{C}$, 10% – 90%-CI, years 2031 – 2041) for Hist/SSP2-4.5 and Hist/SSP5-8.5, respectively (Figures 3e,f).

The magnitude of the B_{surf} trends is not dependent on the historical B_{surf} value and larger B_{surf} trends can be expected for higher emission scenarios (Figure 3c). It should be noted that five CMIP6 models have a positive historical B_{surf} (1850 – 1899, see Table S1). For example, the NESM3 (highest historical B_{surf}) has a very weak historical AMOC strength of 6.8 Sv (Figure 3d) and, in combination with its negative historical F_{ovS} , suggest that the NESM3 reached an ‘AMOC weak’ state upon the historical initialisation. On the other hand, the FGOALS-g3 (lowest historical B_{surf}) has a strong historical AMOC strength of 24.3 Sv and a positive F_{ovS} of 0.36 Sv and its B_{surf} does not change sign.

There is a tendency among the suite of CMIP6 models where models with relatively large B_{surf} have relatively low F_{ovS} values ($R^2 = 0.66$) and weak AMOC strengths ($R^2 = 0.69$) for the historical period. Similar relations in CMIP6 are found for the present-day (1994 – 2020) period and CMIP6 biases in F_{ovS} and AMOC strength influence their responses under climate change [36]. Previous work [37] and the CESM results here (Figures 2 and S3) show that the case with historical positive F_{ovS} and strong AMOC is more resilient under climate change than the case with historical negative F_{ovS} and weak AMOC strength. This indicates that the various model biases [36] upon initialisation set the AMOC sensitivity under the applied forcing.

Excluding the five CMIP6 models with positive historical B_{surf} from the multi-model mean shifts the B_{surf} sign change to 2059 (warming of $+2.27^\circ\text{C}$) and 2050 (warming of $+2.39^\circ\text{C}$) for Hist/SSP2-4.5 and Hist/SSP5-8.5, respectively (Figures 3e,f). For the 19 CMIP6 models with a negative historical B_{surf} , we report that 8 (10) models have switched B_{surf} sign by mid 21st century and 14 (16) models by the end of the 21st century under Hist/SSP2-4.5 (Hist/SSP5-8.5). Based on the B_{surf} responses, we expect that most CMIP6 models will show an AMOC tipping event when integrating the two SSP scenarios beyond 2100.

The Present-day Forcing on the AMOC

Observational data is very limited to determine B_{surf} responses and compare against CMIP6 under climate change. Instead, we use the reanalysis product SODA3.15.2 (1980 – 2022) to analyse B_{surf} responses under present-day climate change. The SODA3.15.2 has a mean AMOC strength of 16.8 Sv (not shown) and its B_{surf} is negative (-0.23 J kg^{-1}) and is increasing (Figure 4a) under climate change by 0.36 J kg^{-1}

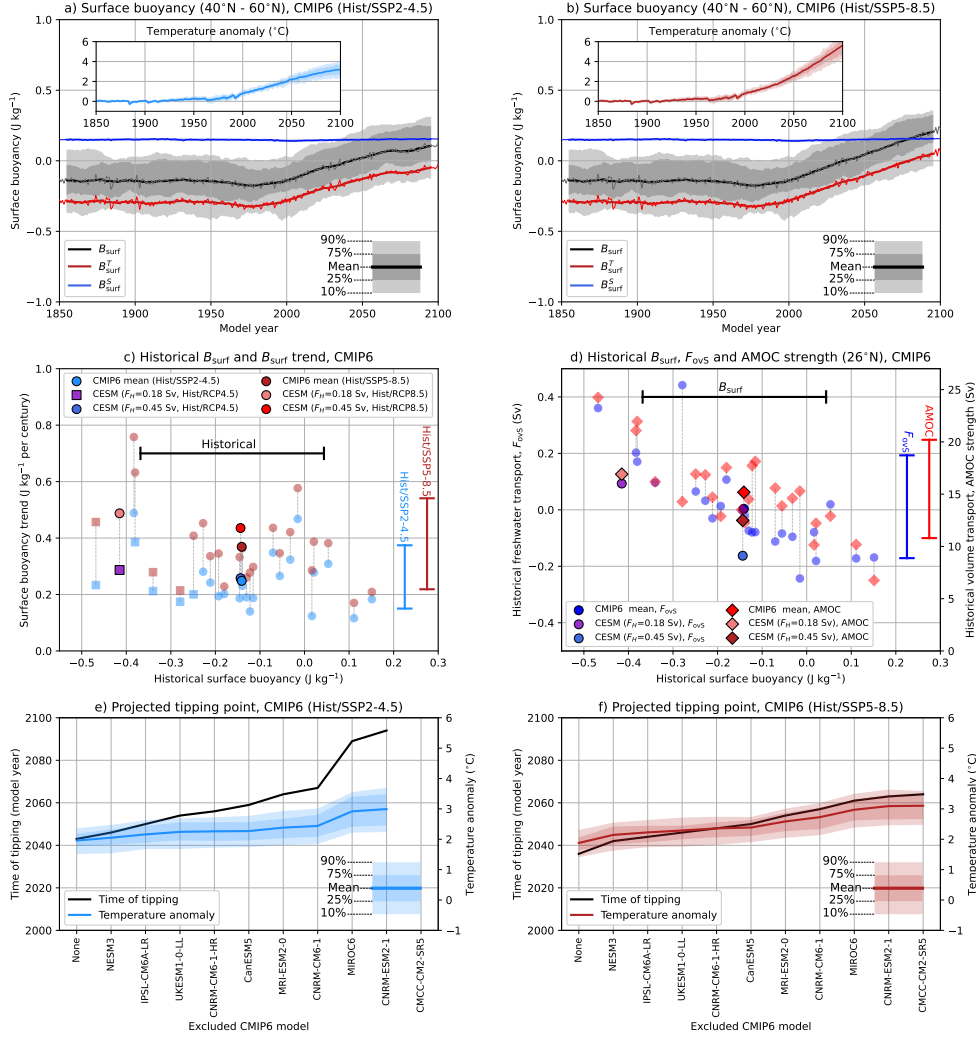


Fig. 3 Surface buoyancy responses in the CMIP6. (a & b): The surface buoyancy (B_{surf}) decomposition for CMIP6 under the Hist/SSP2-4.5 and Hist/SSP5-8.5 scenarios. The multi-model mean and percentiles are smoothed through a 11-year running mean. (c): The 24 CMIP6 models with the historical (1850 – 1899) B_{surf} against the B_{surf} trends (2000 – 2100) for Hist/SSP2-4.5 (blue) and Hist/SSP5-8.5 (red). The error bars indicate the 10% to 90%-CI. The thin lines connect the two forcing scenarios to the same climate model. The four CESM simulations (Figure 2) are also displayed. The circled markers indicate at least one 11-year window with positive B_{surf} , the squared markers indicate that B_{surf} remains negative. (d): Similar to panel c, but now for the historical B_{surf} against the F_{ovs} (circled markers) and AMOC strength (diamond markers). (e & f): The tipping time is determined where the B_{surf} multi-model mean switches sign, using the smoothed time series from panels a and b. The same procedure is repeated by excluding the NESM3 (highest historical B_{surf}) from the multi-model mean, then the IPSL-CM6A-LR and NESM3 are excluded, and so on. The associated temperature anomaly (over the same 11-year window) is also shown.

per century ($p < 0.05$). The CMIP6 multi-model mean has, as explained above, a similar trend under the Hist/SSP5-8.5 scenario (Figure 3b). When we linearly extrapolate

the SODA3.15.2 trend to zero (Figure 4b), we find that B_{surf} changes sign by 2067 and when using the CMIP6 models this is by 2086 (2065 – 2127, 10% – 90%-CI) under Hist/SSP2-4.5 and by 2065 (2052 – 2095, 10% – 90%-CI) under Hist/SSP5-8.5. The associated global warming in the CMIP6 multi-model mean is $+2.99^\circ\text{C}$ ($+2.16^\circ\text{C}$ to $+3.71^\circ\text{C}$, 10% – 90%-CI, years 2081 – 2091) for SSP2-4.5 and $+3.37^\circ\text{C}$ ($+2.52^\circ\text{C}$ to $+3.93^\circ\text{C}$, 10% – 90%-CI, years 2060 – 2070) for SSP5-8.5.

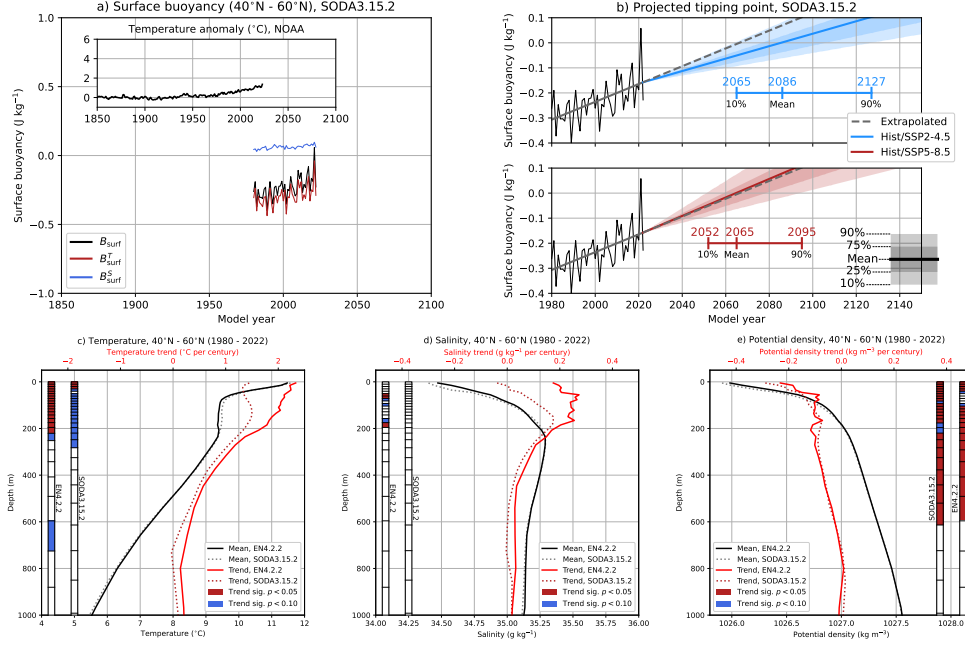


Fig. 4 The tipping point estimate based on surface buoyancy changes under climate change. (a): The surface buoyancy (B_{surf}) decomposition for SODA3.15.2 (1880 – 2022) and the observed yearly-averaged global mean surface temperature anomaly compared to the historical period (1850 – 1899). (b): The linearly extrapolated B_{surf} for SODA3.15.2 (dashed gray curve) and the CMIP6 multi-model mean B_{surf} trend (over the 21st century) for the Hist/SSP2-4.5 and Hist/SSP5-8.5 scenarios. (c – e): The vertical structure of temperature, salinity and potential density over 40°N – 60°N (Atlantic Ocean) and for the period 1980 – 2022. The black (red) curves are the time means (trends) for 1980 – 2022, and are shown for EN4.2.2 and SODA3.15.2. The significance [35] of the trends with depth are displayed on the sides of each panel.

Because a positive B_{surf} is not consistent with the negative present-day B_{surf} found in SODA3.15.2, we exclude the 13 CMIP6 models with a B_{surf} sign change before 2022 in any of the two Hist/SSPs scenarios (Table S1). This results in a B_{surf} sign change by 2084 (2063 – 2107, 10% – 90%-CI, Hist/SSP2-4.5) and by 2060 (2047 – 2079, 10% – 90%-CI, Hist/SSP5-8.5). The associated warming levels in the CMIP6 mean (of 11 models) are now $+2.78^\circ\text{C}$ ($+2.12^\circ\text{C}$ to $+3.45^\circ\text{C}$, 10% – 90%-CI, Hist/SSP2-4.5) and $+2.89^\circ\text{C}$ ($+2.28^\circ\text{C}$ to $+3.40^\circ\text{C}$, 10% – 90%-CI, Hist/SSP5-8.5). The critical temperature anomaly for AMOC tipping is about 3°C and is robust for the two different forcing scenarios. The projected tipping time is found after 2050, but the timing

strongly depends on the forcing scenario. Based on the $+3^{\circ}\text{C}$ warming threshold derived from the SODA3.15.2 extrapolation, none (SSP2-4.5) and only 3 (SSP5-8.5) of the 24 CMIP6 models surpass this threshold by mid century (2045 – 2055) and 15 of the CMIP6 (SSP2-4.5) and all of CMIP6 (SSP5-8.5) surpass it by the end of the century (2090 – 2100).

The positive B_{surf} trend in SODA3.15.2 suggests that the AMOC is weakening under present-day climate change. Another line of evidence of AMOC weakening is the vertical stratification increase over the isopycnal outcropping region (Figures 4c–e), which enhances the upper ocean buoyancy. The time means (1980 – 2022) of SODA3.15.2 are very close to the observational product EN4.2.2. When comparing the temperature and salinity trends between the two products, there are some deviations and these are mainly found in the upper 200 m. These differences cancel out for the potential density trends, which are comparable between the two products and, more importantly, are primarily induced by positive temperature trends. Previous studies [38, 39] and our buoyancy decomposition of the CESM under climate change (Figure S5) demonstrate that global warming enhances the vertical temperature stratification and induces the initial AMOC weakening.

Satellite observations between 1993 and 2020 show the characteristic warming hole south of Greenland (Figure S7) and this has been linked to AMOC weakening [10], but this interpretation has received substantial criticism [13, 40, 41]. The products EN4.2.2 and SODA3.15.2, together with reanalysis products GLORS12V1 and ORAS5, realistically reproduce the observed SST trends over the same period (Figure S7). There are, however, differences in the sea surface salinity trends when comparing the different products. The time mean temperature, salinity and potential density with depth are consistent among the products, whereas the trends are less coherent. The ORAS5 has the largest trend differences compared to EN4.2.2, in particular for salinity, and its surface buoyancy does not show a significant trend over its total available period (1985 – 2023, Figure S8a). The GLORYS12V1 does not provide the required data to determine the surface buoyancy. Both observational and reanalysis products are too short (28 years) to reliably test their significance on the trends. Nevertheless, the results over the 1993 – 2020 period also indicate that positive temperature anomalies dominate the vertical stratification responses under climate change, leading to an increase of the upper ocean buoyancy.

Discussion

In three out of the four climate change CESM simulations shown here we find that the AMOC collapses to a much ($< -80\%$) weaker state. This weaker state is reached after the 21st century but a substantial AMOC weakening occurs already during the 21st century. The initial AMOC weakening under climate change is induced by transient temperature responses [38, 39] and thereafter the dominant salt-advection feedback takes over [42]. The AMOC-induced cooling over Northwestern Europe is strong enough to offset the regional warming under climate change.

We have linked the AMOC collapse to the surface buoyancy over the isopycnal outcropping region in the Atlantic Ocean ($40^{\circ}\text{N} - 60^{\circ}\text{N}$) for which there is a strong

theoretical support [20–22]. By first analysing the quasi-equilibrium hosing simulation (without any climate change), we find that a diagnostic for the AMOC tipping event is the sign change in the characteristic net surface buoyancy loss. The destabilising salt-advection feedback, in combination with surface buoyancy gain, results in an AMOC tipping event in the CESM. Under the high emission scenario (Hist/RCP8.5), the surface buoyancy always changes sign in the 21st century and the AMOC collapses beyond 2100. In the middle-of-the-road scenario (Hist/RCP4.5), the AMOC weakening and surface buoyancy increase are smaller compared to the high emission scenario. In this scenario, depending on the background climate conditions and thus the initial surface buoyancy value, this either results in (partial) AMOC recovery or in a full AMOC collapse.

The reanalysis product SODA3.15.2 shows an increase in the surface buoyancy and vertical stratification and both indicate that the AMOC is weakening under present-day climate change. By linearly extrapolating the CMIP6 projections, the AMOC tipping event occurs by 2065 (Hist/SSP5-8.5) and by 2086 (Hist/SSP2-4.5) and corresponds to a global warming of about +3°C (+2.2°C to +3.9°C, 10% – 90%-CI). More than half of the CMIP6 models under SSP2-4.5 surpasses the +3°C warming threshold by the end of the century and all of them under SSP5-8.5, indicating that there is a substantial risk of AMOC tipping under moderate climate change. The full AMOC collapse develops after 2100 and it is therefore important to simulate to at least 2200 in the next generation climate models of CMIP phase 7.

The quantity F_{ovS} is an important diagnostic and a negative F_{ovS} sign appears to be connected to the salt-advection feedback strength [6, 30–33]. Note that this quantity can only be used under quasi-equilibrium conditions and these conditions include the equilibration of the lower level interior basin [39] in response to an imposed anomaly. However, if the deep ocean has no time to equilibrate as a result of a large freshwater flux change [4, 34] or rapid climate change, the F_{ovS} sign is a less clear indicator of the salt-advection feedback. Until now, the observed AMOC decline is only gradual [10–14] and the negative F_{ovS} trend [6] is still a useful early warning indicator. Alternatively, the surface buoyancy is linked to the F_{ovS} and AMOC strength and can be used under strong transient conditions as collapse indicator. These relations are found for the historical period, the present-day (1994 – 2020) period [36] and in a strongly eddying version of the CESM (Figure S8b). The bottom line is that climate model biases [32, 36, 37, 43–47] need to be reduced to have a realistic AMOC sensitivity under climate change.

Recent AMOC studies have (indirectly) questioned the sixth IPCC report’s statement [19] on the possibility of an AMOC collapse before 2100 [6, 15, 36, 48]. Our study demonstrates again that the present-day AMOC is on route to tipping. The previous critical temperature threshold of +4°C (+1.4°C to +8.0°C) warming [2] was based on enhanced ice and river run-off [1, 49] and the results from a few CMIP phase 5 models [50, 51]. We link AMOC dynamics to the surface buoyancy and, by using reanalysis and 24 different CMIP6 models, we arrive at a critical temperature threshold of +3°C (+2.2°C to +3.9°C) warming for causing an AMOC tipping event. Under high emission scenarios this temperature threshold will be reached after 2050 and is in agreement with previous estimates [16, 17]. Note that these temperature thresholds

are upper bounds as enhanced Greenland Ice Sheet melt under future warming is not considered in the CESM nor CMIP6. A positive note is that a lower emission scenario can delay or prevent an AMOC collapse, as was demonstrated for the CESM here. To limit the risk of a potential AMOC collapse in the foreseeable future, global society needs to be on track of a low emission scenario (i.e., SSP1-1.9 and SSP1-2.6) and urgent climate action is needed to guarantee this.

Methods

Climate Model Simulations. The CESM is a fully-coupled climate model and has horizontal resolutions of 1° for the ocean/sea-ice components and 2° for the atmosphere/land model components. Mesoscale features such as ocean eddies are parameterised. We imposed a slowly-varying freshwater flux forcing (i.e., quasi-equilibrium approach) over the North Atlantic Ocean ($20^\circ\text{N} - 50^\circ\text{N}$) and compensated elsewhere to conserve the total ocean salinity [6]. From the quasi-equilibrium simulation, we branched off two simulations under their constant freshwater flux forcing of $F = 0.18$ Sv and $F = 0.45$ Sv to find statistical equilibria [28]. From the end of these statistical equilibria simulations, we imposed the historical forcing (1850 – 2005) followed by either the RCP4.5 or RCP8.5 scenario (2006 – 2100) and with a constant freshwater flux forcing ($F = 0.18$ Sv or $F = 0.45$ Sv).

The high-resolution version of the CESM was retained from the iHESP project [52] under the Hist/RCP8.5 scenario (and no freshwater flux forcing). The high-resolution CESM version has a 0.1° for the ocean/sea-ice components and 0.25° for the atmosphere/land model components, and explicitly resolves ocean eddies and tropical cyclones. A companion low-resolution version of the CESM is available with the iHESP project, however, not all relevant variables were stored to determine the surface buoyancy and hence we did not include this simulation in our analysis.

For the CMIP6 models, we retained the historical forcing (1850 – 2014) followed by the SSP2-4.5 and SSP5-8.5 (2015 – 2100) scenarios. Note that the forcing scenarios are slightly different between the CESM simulations (the RCPs) and CMIP6 (the SSPs). We retained the sea surface temperature ('tos'), sea surface salinity ('sos'), total heat flux ('hfds'), total freshwater flux ('wfo'), meridional velocity ('vo'), salinity ('so') and surface air temperature ('tas'). Only 24 models (Table S1) provided all seven variables for the different forcing scenarios and we selected one realisation ('r1i1p1f1' or 'r1i1p1f2') for each CMIP6 model, the analysis is conducted on their native grid.

The observational product EN4.2.2 (horizontal resolution of $1^\circ \times 1^\circ$, 1900 – 2023) assimilates observations from various sources [53]. The reanalysis products are steered towards observations and the products are the SODA3.15.2 (horizontal resolution of $1/4^\circ \times 1/4^\circ$, 1980 – 2022), the GLORYS12V1 (horizontal resolution of $1/12^\circ \times 1/12^\circ$, 1993 – 2020) and the ORAS5 (horizontal resolution of $1/4^\circ \times 1/4^\circ$, 1958 – 2023).

The AMOC strength. The AMOC strength is defined as the total meridional volume transport at 26°N over the upper 1,000 m:

$$\text{AMOC}(y = 26^\circ\text{N}) = \int_{-1000}^0 \int_{x_W}^{x_E} v \, dx dz \quad (1)$$

When thermal wind balance is applicable for the AMOC (AMOC_{TWB}), its strength can be approximated by [20, 54]:

$$\partial_{zz}\Psi = \frac{g}{\rho_0 f} (\sigma_b(z) - \sigma_n(z)) \quad (2)$$

with $g = 9.8 \text{ m s}^{-2}$, $\rho_0 = 1027 \text{ kg m}^{-3}$, $f = 1.2 \times 10^{-4} \text{ s}^{-1}$. The terms σ_b and σ_n represent the (spatially-averaged) potential density over the Atlantic basin ($34^\circ\text{S} - 40^\circ\text{N}$) and the isopycnal outcropping region ($40^\circ\text{N} - 60^\circ\text{N}$) with depth. The AMOC_{TWB} represents the AMOC strength over the isopycnal outcropping region ($\approx 50^\circ\text{N}$) and captures variability on decadal to centennial time scales. We determined the AMOC_{TWB} at 1,000 m depth (Figures S1e,f). The potential densities are determined using the Thermodynamic Equation of SeaWater 2010 (TEOS-10) toolkit [55], which uses ocean temperature and salinity as input. Note that the CESM provides the potential density as standard output, but for consistency with the buoyancy calculation (see below) and other reanalysis products which do not provide the potential density as standard output, we used the TEOS-10 toolkit.

Oceanic Buoyancy. The ocean buoyancy and surface buoyancy [56] are defined as:

$$B_{\text{ocean}}(T, S) = \frac{g}{\rho_0} \int_{z_1}^{z_2} (\sigma(z) - \sigma(z=0)) dz \quad (3a)$$

$$B_{\text{surf}} = \frac{g\alpha}{\rho_0 C_p} Q_{\text{heat}} + \beta g S_{\text{surf}} Q_{\text{fresh}} = B_{\text{surf}}^T + B_{\text{surf}}^S \quad (3b)$$

where σ is the potential density (in kg m^{-3}), α the thermal expansion coefficient (in K^{-1}), C_p the oceanic heat capacity (in $\text{J kg}^{-1} \text{K}^{-1}$), Q_{heat} the net heat input into the ocean (in J), β the haline contraction coefficient (in kg g^{-1}), S_{surf} the sea surface salinity (in g kg^{-1}) and Q_{fresh} the net freshwater input into the ocean (in m). The term Q_{heat} (Q_{fresh}) can be further decomposed in, for example, the contribution by longwave radiation and sensible heat fluxes (evaporation and freshwater flux forcing).

The temperature (salinity) contribution to ocean buoyancy changes can be determined by using a reference salinity (temperature) and is indicated by $B_{\text{ocean}}(T, \bar{S}) = B_{\text{ocean}}^T$ ($B_{\text{ocean}}(\bar{T}, S) = B_{\text{ocean}}^S$). The monthly-averaged references are determined over the first 50 years of the hosing simulation and the historical period (1850 – 1899). The sea water properties (e.g., α , C_p , etc.) are determined using TEOS-10. The ocean buoyancy and surface buoyancy are determined with monthly-averaged model output and are then converted to yearly averages and yearly sums, respectively.

The Freshwater Transport. The freshwater transport carried by the overturning component at 34°S (F_{ovS}) is determined as:

$$F_{\text{ovS}} = F_{\text{ov}}(y = 34^\circ\text{S}) = -\frac{1}{S_0} \int_{-H}^0 \left[\int_{x_W}^{x_E} v^* dx \right] [\langle S \rangle - S_0] dz \quad (4)$$

where $S_0 = 35 \text{ g kg}^{-1}$ is a reference salinity. The v^* is defined as $v^* = v - \hat{v}$, where v is the meridional velocity and \hat{v} the full-depth section spatially-averaged meridional velocity. The quantity $\langle S \rangle$ indicate the zonally-averaged salinity and primed quantities (v' and S') are deviations from their respective zonal means.

Acknowledgments. The model simulation and the analysis of all the model output was conducted on the Dutch National Supercomputer Snellius within NWO-SURF project 17239.

Declarations

- Funding – R.M.v.W., E.Y.P.V. and H.A.D. are funded by the European Research Council through the ERC-AdG project TAOC (project 101055096).
- Conflict of interest – The authors declare no competing interest
- Ethics approval – Not applicable
- Availability of data and materials – The (processed) model output will be made available on Zenodo upon publication. The reanalysis and assimilation products can be accessed through: SODA3.15.2 (<http://www.soda.umd.edu>), EN4.2.2.g10 (<https://www.metoffice.gov.uk/hadobs/en4/>), GLO-RYS12V1 (<https://doi.org/10.48670/moi-00021>) and ORAS5 (<https://doi.org/10.24381/cds.67e8eeb7>). The observational products are found through: sea surface temperature observations (version 2.1, Level 4, <https://doi.org/10.24381/cds.cf608234>), sea surface salinity observations (Level 4, <https://doi.org/10.48670/moi-00051>) and observed global mean surface temperature anomalies (version 6, <https://www.ncei.noaa.gov/data/noaa-global-surface-temperature/v6/access/timeseries/>) The CMIP6 model output is provided by the World Climate Research Programme’s Working Group on Coupled Modelling.
- Code availability – The analysis scripts will be made available on Zenodo upon publication.
- Authors’ contributions – R.M.v.W., E.Y.P.V. and H.A.D. conceived the idea for this study. M.K. performed the model simulation with the CESM. R.M.v.W. conducted the analysis and prepared all figures. All authors were actively involved in the interpretation of the analysis results and the writing process.

References

- [1] Lenton, T.M., Held, H., Kriegler, E., Hall, J.W., Lucht, W., Rahmstorf, S., Schellnhuber, H.J.: Tipping elements in the Earth’s climate system. *Proceedings of the National Academy of Sciences of the United States of America* **105**(6), 1786–93 (2008) <https://doi.org/10.1073/pnas.0705414105>
- [2] Armstrong McKay, D.I., Staal, A., Abrams, J.F., Winkelmann, R., Sakschewski, B., Loriani, S., Fetzer, I., Cornell, S.E., Rockström, J., Lenton, T.M.: Exceeding 1.5 C global warming could trigger multiple climate tipping points. *Science* **377**(6611), 7950 (2022)

- [3] Johns, W.E., Baringer, M.O., Beal, L., Cunningham, S., Kanzow, T., Bryden, H.L., Hirschi, J., Marotzke, J., Meinen, C., Shaw, B., *et al.*: Continuous, array-based estimates of Atlantic Ocean heat transport at 26.5 N. *Journal of Climate* **24**(10), 2429–2449 (2011)
- [4] Orihuela-Pinto, B., England, M.H., Taschetto, A.S.: Interbasin and interhemispheric impacts of a collapsed atlantic overturning circulation. *Nature Climate Change* **12**(6), 558–565 (2022)
- [5] Westen, R.M., Dijkstra, H.A.: Asymmetry of AMOC Hysteresis in a State-Of-The-Art Global Climate Model. *Geophysical Research Letters* **50**(22), 2023–106088 (2023)
- [6] Westen, R.M., Kliphuis, M., Dijkstra, H.A.: Physics-based early warning signal shows that AMOC is on tipping course. *Science advances* **10**(6), 1189 (2024)
- [7] Garzoli, S.L., Baringer, M.O., Dong, S., Perez, R.C., Yao, Q.: South Atlantic meridional fluxes. *Deep Sea Research Part I: Oceanographic Research Papers* **71**, 21–32 (2013)
- [8] Srokosz, M.A., Bryden, H.L.: Observing the Atlantic Meridional Overturning Circulation yields a decade of inevitable surprises. *Science* **348**(6241), 1255575–1255575 (2015) <https://doi.org/10.1126/science.1255575>
- [9] Lozier, M.S., Li, F., Bacon, S., Bahr, F., Bower, A.S., Cunningham, S., Jong, M.F., Steur, L., deYoung, B., Fischer, J., *et al.*: A sea change in our view of overturning in the subpolar north atlantic. *Science* **363**(6426), 516–521 (2019)
- [10] Caesar, L., Rahmstorf, S., Robinson, A., Feulner, G., Saba, V.: Observed fingerprint of a weakening Atlantic Ocean overturning circulation. *Nature* **556**(7700), 191–196 (2018) <https://doi.org/10.1038/s41586-018-0006-5>
- [11] Estella-Perez, V., Mignot, J., Guilyardi, E., Swingedouw, D., Reverdin, G.: Advances in reconstructing the amoc using sea surface observations of salinity. *Climate Dynamics* **55**, 975–992 (2020)
- [12] Caesar, L., McCarthy, G.D., Thornalley, D.J.R., Cahill, N., Rahmstorf, S.: Current Atlantic Meridional Overturning Circulation weakest in last millennium. *Nature Geoscience* **14**(3), 118–120 (2021) <https://doi.org/10.1038/s41561-021-00699-z>
- [13] Worthington, E.L., Moat, B.I., Smeed, D.A., Mecking, J.V., Marsh, R., McCarthy, G.D.: A 30-year reconstruction of the Atlantic meridional overturning circulation shows no decline. *Ocean Science* **17**(1), 285–299 (2021)
- [14] Michel, S., Dijkstra, H., Guardamagna, F., Jacques-Dumas, V., Westen, R., Heydt, A.: Deep learning reconstruction of atlantic meridional overturning

circulation strength validates ongoing twenty-first century decline. (2023)

- [15] Boers, N.: Observation-based early-warning signals for a collapse of the Atlantic Meridional Overturning Circulation. *Nature Climate Change* **11**(8), 680–688 (2021) <https://doi.org/10.1038/s41558-021-01097-4>
- [16] Ditlevsen, P., Ditlevsen, S.: Warning of a forthcoming collapse of the Atlantic meridional overturning circulation. *Nature Communications* **14**(1), 4254 (2023)
- [17] Smolders, E.J.V., Westen, R.M., Dijkstra, H.A.: Probability estimates of a 21st century amoc collapse (2024) [arXiv:2406.11738](https://arxiv.org/abs/2406.11738) [physics.ao-ph]
- [18] Weijer, W., Cheng, W., Garuba, O.A., Hu, A., Nadiga, B.T.: CMIP6 Models Predict Significant 21st Century Decline of the Atlantic Meridional Overturning Circulation. *Geophysical Research Letters* **47**(12), 2019–08607 (2020) <https://doi.org/10.1029/2019gl086075>
- [19] Fox-Kemper, B., Hewitt, H.T., Xiao, C., co-authors: Ocean, cryosphere and sea level change. in *climate change 2021: The physical science basis. contribution of working group i to the sixth assessment report of the intergovernmental panel on climate change*, 1211–1362 (2021) <https://doi.org/10.1017/9781009157896.011>
- [20] Nikurashin, M., Vallis, G.: A theory of the interhemispheric meridional overturning circulation and associated stratification. *Journal of Physical Oceanography* **42**(10), 1652–1667 (2012)
- [21] Wolfe, C.L., Cessi, P.: Salt feedback in the adiabatic overturning circulation. *Journal of Physical Oceanography* **44**(4), 1175–1194 (2014)
- [22] Wolfe, C.L., Cessi, P.: Multiple regimes and low-frequency variability in the quasi-adiabatic overturning circulation. *Journal of Physical Oceanography* **45**(6), 1690–1708 (2015)
- [23] Walin, G.: On the relation between sea-surface heat flow and thermal circulation in the ocean. *Tellus* **34**(2), 187–195 (1982)
- [24] Marshall, J., Jamous, D., Nilsson, J.: Reconciling thermodynamic and dynamic methods of computation of water-mass transformation rates. *Deep Sea Research Part I: Oceanographic Research Papers* **46**(4), 545–572 (1999)
- [25] Marotzke, J.: Abrupt climate change and thermohaline circulation: Mechanisms and Predictability. *Proc. Natl. Acad. Sci.* **97**, 1347–1350 (2000)
- [26] Peltier, W.R., Vettoretti, G.: Dansgaard-Oeschger oscillations predicted in a comprehensive model of glacial climate: A “kicked” salt oscillator in the Atlantic. *Geophysical Research Letters* **41**(20), 7306–7313 (2014)

- [27] Lin, Y.-J., Rose, B.E., Hwang, Y.-T.: Mean state AMOC affects AMOC weakening through subsurface warming in the Labrador Sea. *Journal of Climate* **36**(12), 3895–3915 (2023)
- [28] Westen, R.M., Jacques-Dumas, V., Boot, A.A., Dijkstra, H.A.: The Role of Sea-ice Processes on the Probability of AMOC Transitions. <https://doi.org/10.48550/arXiv.2401.12615> (2024)
- [29] Smeed, D.A., Josey, S., Beaulieu, C., Johns, W., Moat, B.I., Frajka-Williams, E., Rayner, D., Meinen, C.S., Baringer, M.O., Bryden, H.L., *et al.*: The North Atlantic Ocean is in a state of reduced overturning. *Geophysical Research Letters* **45**(3), 1527–1533 (2018)
- [30] Dijkstra, H.A.: Characterization of the multiple equilibria regime in a global ocean model. *Tellus A: Dynamic Meteorology and Oceanography* **59**(5), 695–705 (2007)
- [31] Huisman, S.E., Den Toom, M., Dijkstra, H.A., Drijfhout, S.: An indicator of the multiple equilibria regime of the atlantic meridional overturning circulation. *Journal of Physical Oceanography* **40**(3), 551–567 (2010)
- [32] Mecking, J., Drijfhout, S., Jackson, L., Andrews, M.: The effect of model bias on Atlantic freshwater transport and implications for AMOC bi-stability. *Tellus A: Dynamic Meteorology and Oceanography* **69**(1), 1299910 (2017)
- [33] Weijer, W., Cheng, W., Drijfhout, S.S., Fedorov, A.V., Hu, A., Jackson, L.C., Liu, W., McDonagh, E., Mecking, J., Zhang, J.: Stability of the Atlantic Meridional Overturning Circulation: A review and synthesis. *Journal of Geophysical Research: Oceans* **124**(8), 5336–5375 (2019)
- [34] Jackson, L.C., Asenjo, E., Bellomo, K., Danabasoglu, G., Haak, H., Hu, A., Jungclaus, J., Lee, W., Meccia, V.L., Saenko, O., *et al.*: Understanding AMOC stability: the North Atlantic hosing model intercomparison project. *Geoscientific Model Development Discussions* **2022**, 1–32 (2022)
- [35] Santer, B.D., Wigley, T., Boyle, J., Gaffen, D.J., Hnilo, J., Nychka, D., Parker, D., Taylor, K.: Statistical significance of trends and trend differences in layer-average atmospheric temperature time series. *Journal of Geophysical Research: Atmospheres* **105**(D6), 7337–7356 (2000)
- [36] Van Westen, R.M., Dijkstra, H.A.: Persistent climate model biases in the atlantic ocean’s freshwater transport. *Ocean Science* **20**(2), 549–567 (2024)
- [37] Liu, W., Xie, S.-P., Liu, Z., Zhu, J.: Overlooked possibility of a collapsed Atlantic Meridional Overturning Circulation in warming climate. *Science Advances* **3**(1), 1601666 (2017) <https://doi.org/10.1126/sciadv.1601666>
- [38] Levang, S.J., Schmitt, R.W.: What causes the AMOC to weaken in CMIP5?

- [39] Bonan, D.B., Thompson, A.F., Newsom, E.R., Sun, S., Rugenstein, M.: Transient and equilibrium responses of the Atlantic overturning circulation to warming in coupled climate models: The role of temperature and salinity. *Journal of Climate* **35**(15), 5173–5193 (2022)
- [40] Little, C.M., Zhao, M., Buckley, M.W.: Do surface temperature indices reflect centennial-timescale trends in Atlantic meridional overturning circulation strength? *Geophysical Research Letters* **47**(22), 2020–090888 (2020)
- [41] He, C., Clement, A.C., Cane, M.A., Murphy, L.N., Klavans, J.M., Fenske, T.M.: A North Atlantic warming hole without ocean circulation. *Geophysical research letters* **49**(19), 2022–100420 (2022)
- [42] Gérard, J., Crucifix, M.: Diagnosing the causes of AMOC slowdown in a coupled model: a cautionary tale. *Earth System Dynamics* **15**(2), 293–306 (2024)
- [43] Jackson, L.C.: Shutdown and recovery of the AMOC in a coupled global climate model: The role of the advective feedback. *Geophysical Research Letters* **40**(6), 1182–1188 (2013) <https://doi.org/10.1002/grl.50289>
- [44] Drijfhout, S.S., Weber, S.L., Swaluw, E.: The stability of the MOC as diagnosed from model projections for pre-industrial, present and future climates. *Climate Dynamics* **37**(7-8), 1575–1586 (2011) <https://doi.org/10.1007/s00382-010-0930-z>
- [45] Mecking, J., Drijfhout, S.S., Jackson, L.C., Graham, T.: Stable amoc off state in an eddy-permitting coupled climate model. *Climate Dynamics* **47**, 2455–2470 (2016)
- [46] Bonan, D., Thompson, A., Schneider, T., Zanna, L., Armour, K., Sun, S.: Constraints imply limited future weakening of atlantic meridional overturning circulation. Preprint, <https://doi.org/10.21203/rs.3.rs-4456168/v1> (2024)
- [47] Dijkstra, H.A., Westen, R.M.: The Effect of Indian Ocean Surface Freshwater Flux Biases On the Multi-Stable Regime of the AMOC. *Tellus A: Dynamic Meteorology and Oceanography* **76**(1) (2024)
- [48] Lohmann, J., Dijkstra, H.A., Jochum, M., Lucarini, V., Ditlevsen, P.D.: Multistability and intermediate tipping of the atlantic ocean circulation. *Science Advances* **10**(12), 4253 (2024)
- [49] Rahmstorf, S., Crucifix, M., Ganopolski, A., Goosse, H., Kamenkovich, I., Knutti, R., Lohmann, G., March, R., Mysak, L., Wang, Z., Weaver, A.J.: Thermohaline circulation hysteresis: a model intercomparison. *Geophysical Research Letters* **L23605**, 1–5 (2005)

- [50] Drijfhout, S., Bathiany, S., Beaulieu, C., Brovkin, V., Claussen, M., Huntingford, C., Scheffer, M., Sgubin, G., Swingedouw, D.: Catalogue of abrupt shifts in intergovernmental panel on climate change climate models. *Proceedings of the National Academy of Sciences* **112**(43), 5777–5786 (2015)
- [51] Sgubin, G., Swingedouw, D., Drijfhout, S., Mary, Y., Bennabi, A.: Abrupt cooling over the north atlantic in modern climate models. *Nature Communications* **8**(1), 14375 (2017)
- [52] Chang, P., Zhang, S., Danabasoglu, G., Yeager, S.G., Fu, H., Wang, H., Castruccio, F.S., Chen, Y., Edwards, J., Fu, D., *et al.*: An unprecedented set of high-resolution earth system simulations for understanding multiscale interactions in climate variability and change. *Journal of Advances in Modeling Earth Systems* **12**(12), 2020–002298 (2020)
- [53] Gouretski, V., Reseghetti, F.: On depth and temperature biases in bathythermograph data: Development of a new correction scheme based on analysis of a global ocean database. *Deep Sea Research Part I: Oceanographic Research Papers* **57**(6), 812–833 (2010)
- [54] Jansen, M.F., Nadeau, L.-P., Merlis, T.M.: Transient versus equilibrium response of the ocean’s overturning circulation to warming. *Journal of Climate* **31**(13), 5147–5163 (2018)
- [55] McDougall, T.J., Barker, P.M.: Getting started with TEOS-10 and the Gibbs Seawater (GSW) oceanographic toolbox. *Scor/iapso WG* **127**(532), 1–28 (2011)
- [56] Biló, T., Straneo, F., Holte, J., Le Bras, I.-A.: Arrival of new great salinity anomaly weakens convection in the Irminger Sea. *Geophysical Research Letters* **49**(11), 2022–098857 (2022)
- [57] Arumí-Planas, C., Dong, S., Perez, R., Harrison, M.J., Farneti, R., Hernández-Guerra, A.: A multi-data set analysis of the freshwater transport by the Atlantic meridional overturning circulation at nominally 34.5 S. *Journal of Geophysical Research: Oceans* **129**(6), 2023–020558 (2024)

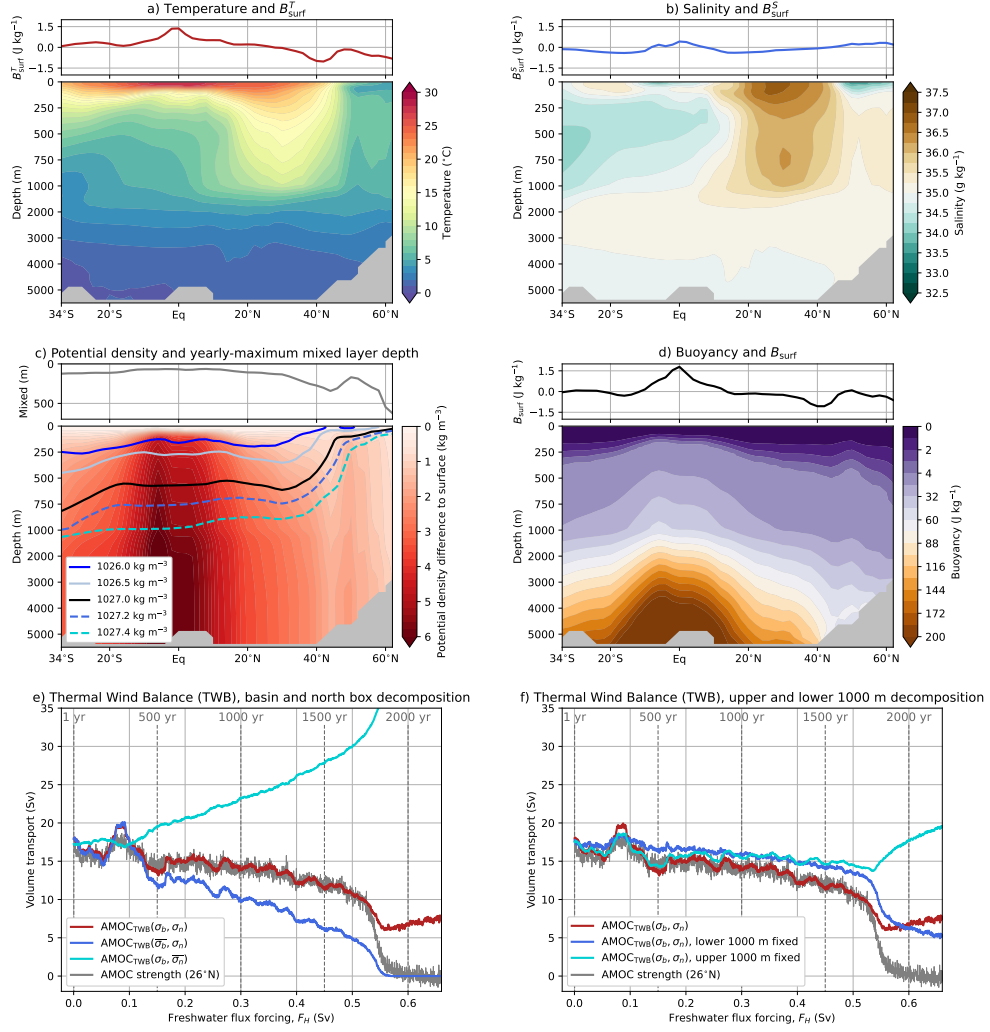


Fig. S1 Atlantic Ocean water properties for the CESM (hosing). (a – d): The zonally-averaged (Atlantic basin) and yearly-averaged temperature, salinity, potential density and ocean buoyancy for the first 50 years of the hosing. The top panels show the yearly-summed surface buoyancy components and the yearly-maximum mixed layer depth. Panel c shows the potential density difference with respect to the surface and the curves represent various isopycnals. (e): The thermal wind balance AMOC approximation ($AMOC_{TWB}(\sigma_b, \sigma_n)$, see Methods) under the hosing. The thermal wind balance is decomposed into a component for which the reference (i.e., first 50 model years) basin box potential density ($AMOC_{TWB}(\bar{\sigma}_b, \sigma_n)$) is used, and the reference north box potential density ($AMOC_{TWB}(\sigma_b, \bar{\sigma}_n)$) is used. We also show the AMOC strength at 1,000 m and 26°N for comparison. (f): Similar to panel e, but now the potential densities over the lower 1,000 m are fixed (i.e., first 50 model years) and the upper 1,000 m are fixed.

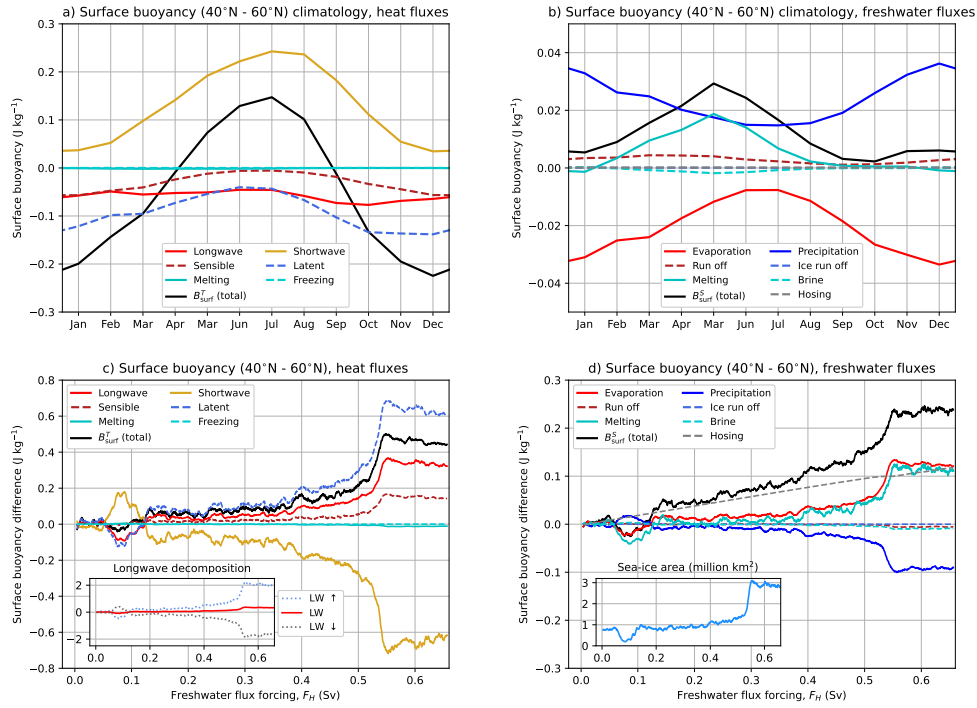


Fig. S2 Surface buoyancy decomposition for the CESM (hosing). (a – b): Climatology over the first 50 model years of the surface buoyancy (40°N – 60°N, Atlantic Ocean) and is decomposed into its different contributions for the (a): heat fluxes and (b): freshwater fluxes. (c – d): The surface buoyancy difference (with respect to the climatology) under the varying freshwater flux forcing for the (c): heat fluxes and (d): freshwater fluxes. The time series are displayed as yearly sums and are smoothed through a 25-year running mean to reduce the variability. The inset in panel c shows the upwelling longwave (LW \uparrow) and the downwelling longwave (LW \downarrow) contributions. The inset in panel d shows the yearly-averaged sea-ice area (grid cells with sea-ice fractions of at least 15%) between 40°N – 60°N. Note the different vertical ranges for the panels.

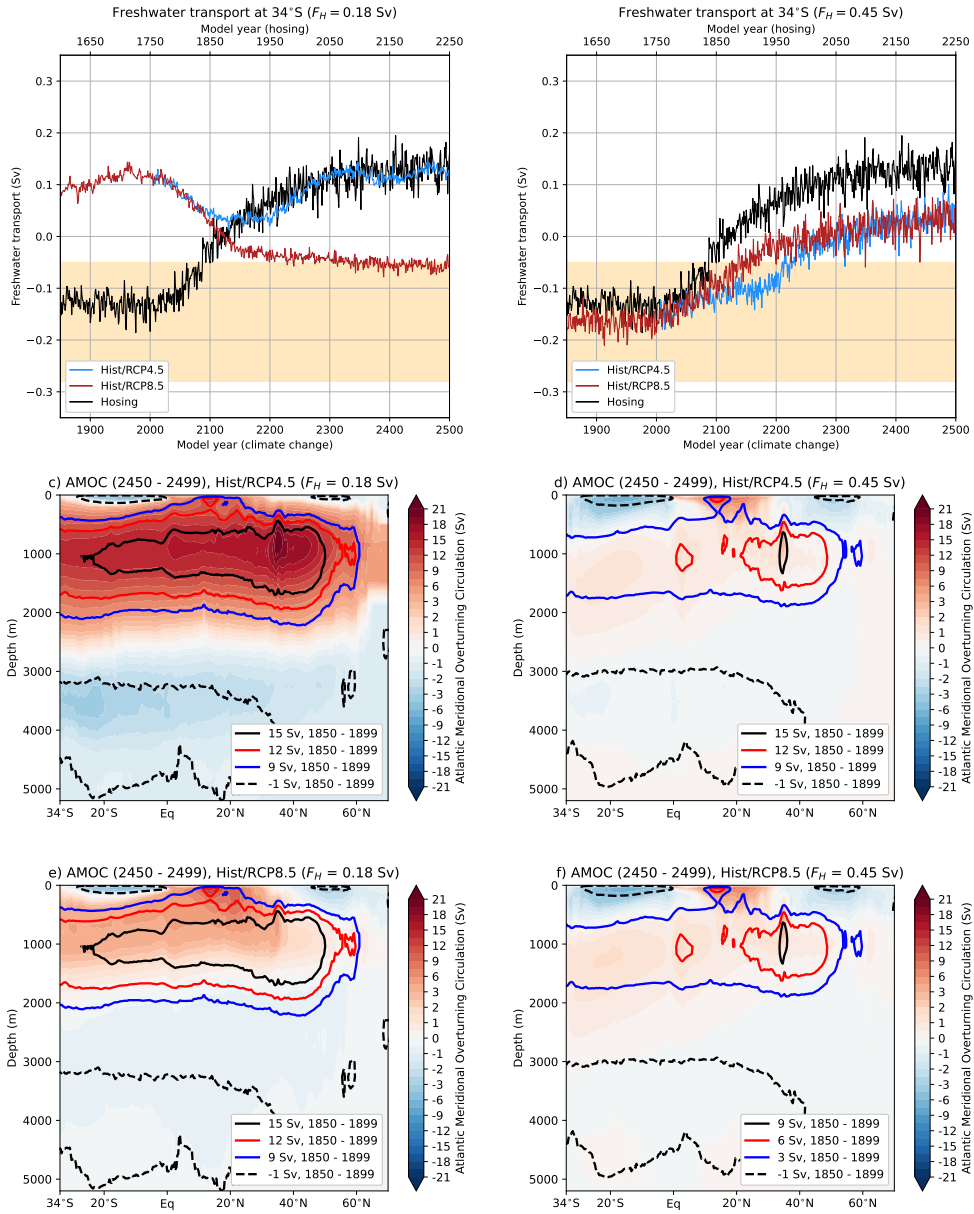


Fig. S3 Atlantic Meridional Overturning Circulation (AMOC) properties. (a & b): The freshwater transport carried by the AMOC at 34°S, F_{OVS} . For reference, the F_{OVS} under the hosing is also shown and is centred around the AMOC tipping event (black curve, top x-axis). The yellow shading indicates observed F_{OVS} values [7, 32, 57]. (b – f): The AMOC streamfunction over the last 50 years (model years 2450 – 2499). The contours indicate the isolines for different AMOC values for the historical period (model years 1850 – 1899).

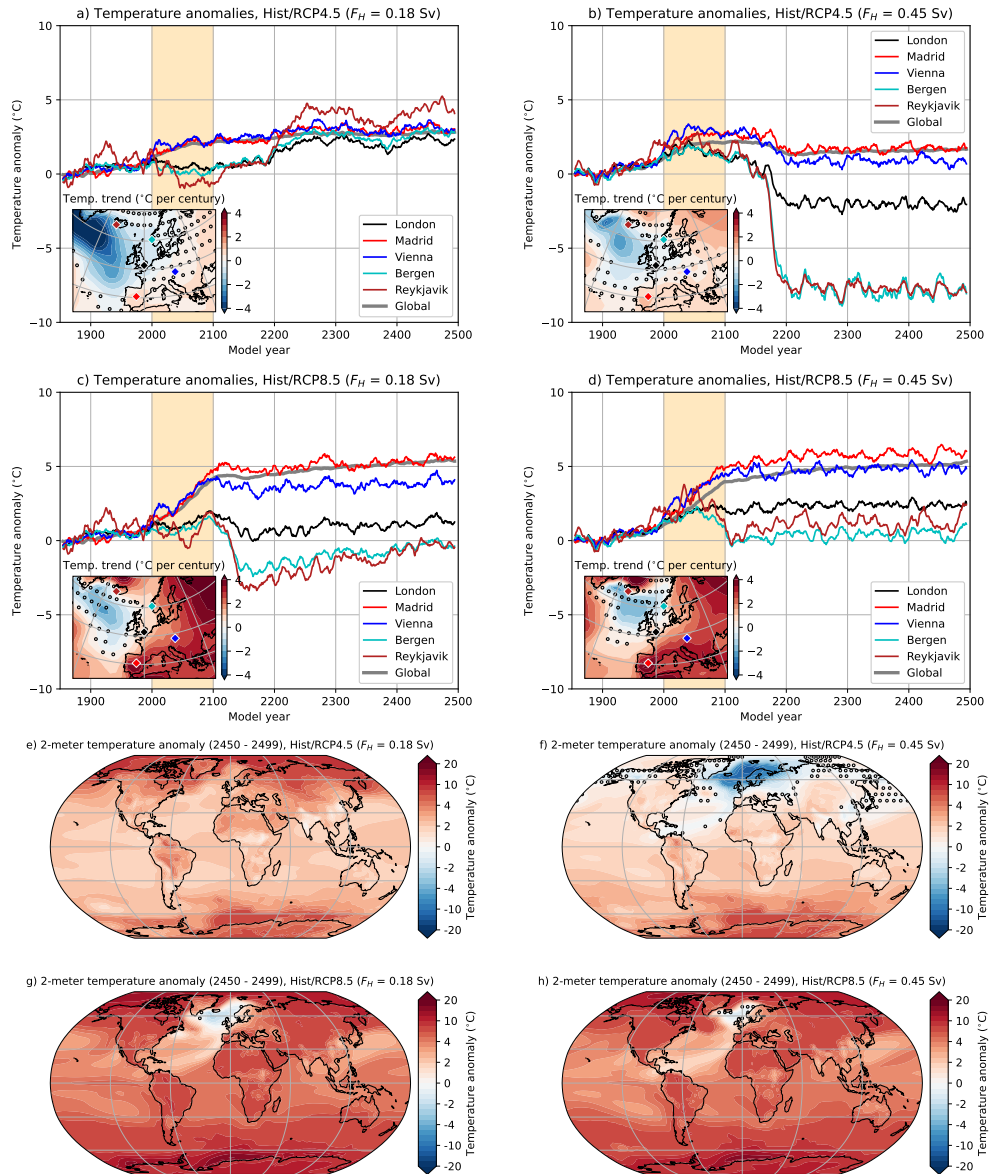


Fig. S4 The surface temperature responses under climate change. (a – d): The yearly-averaged surface temperatures for five different cities (diamond markers in inset) and the global mean under the two climate change scenarios (Hist/RCP4.5 and Hist/RCP8.5) and for $F_H = 0.18$ Sv and $F_H = 0.45$ Sv. The time series are displayed as anomalies compared to the historical period (1850 – 1899) and are then smoothed through a 11-year running mean. The yellow shading indicates the 21st century over which the trends are displayed in the insets, the circled markers indicate non-significant ($p \geq 0.05$, [35]) trends. (e – h): The equilibrium temperature anomalies (compared to 1850 – 1899) at the end of the simulations, the circled markers indicate non-significant ($p \geq 0.05$, two-sided Welch's t-test) differences.

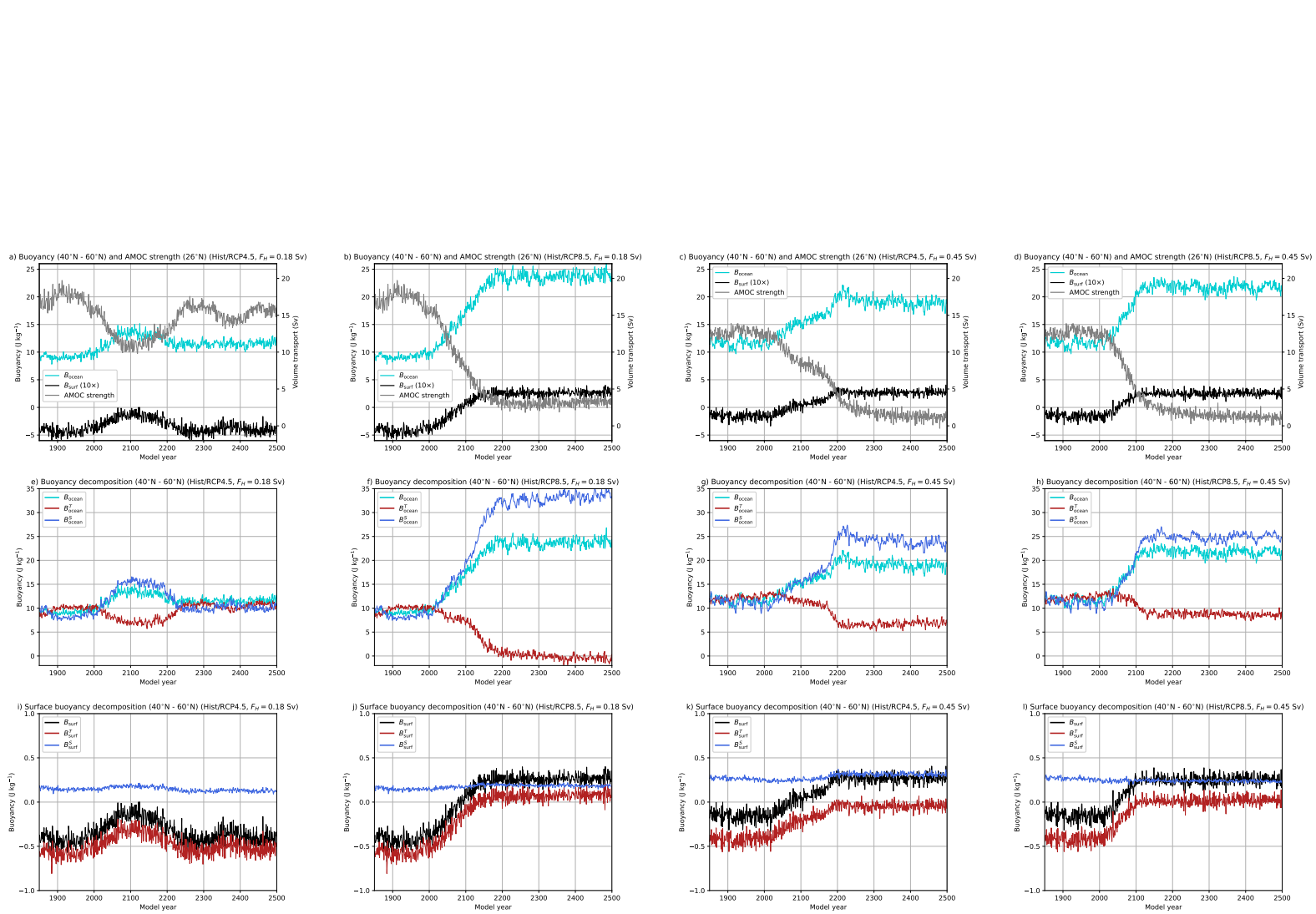


Fig. S5 Buoyancy and AMOC responses under climate change. Similar to Figure 1, but now under the two climate change scenarios (Hist/RCP4.5 and Hist/RCP8.5) and for $F_H = 0.18$ Sv and $F_H = 0.45$ Sv. The climatologies are shown in Figure S6.

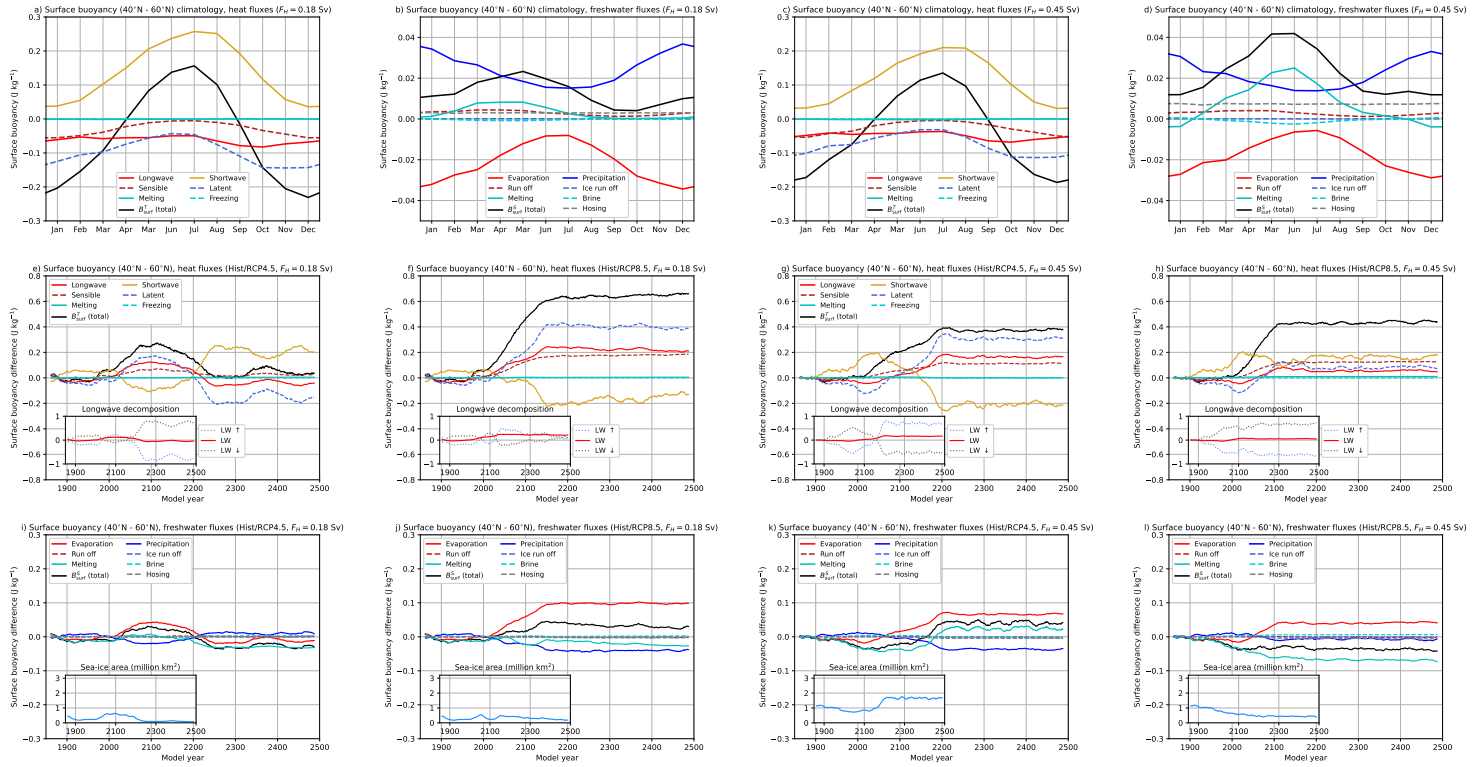


Fig. S6 Surface buoyancy decomposition under climate change. Similar to Figure S2, but now for the different climate change simulations. The climatology (panels a – d) is determined over model years 1850 – 1899. The time series for the heat fluxes are shown in panels e – h and for the freshwater fluxes in panels i – l. Note that there are two historical simulations (for $F_H = 0.18$ Sv and $F_H = 0.45$ Sv) and hence the climatology and the model output between model years 1850 – 2005 are identical when comparing the two climate change scenarios (RCP4.5 and RCP8.5).

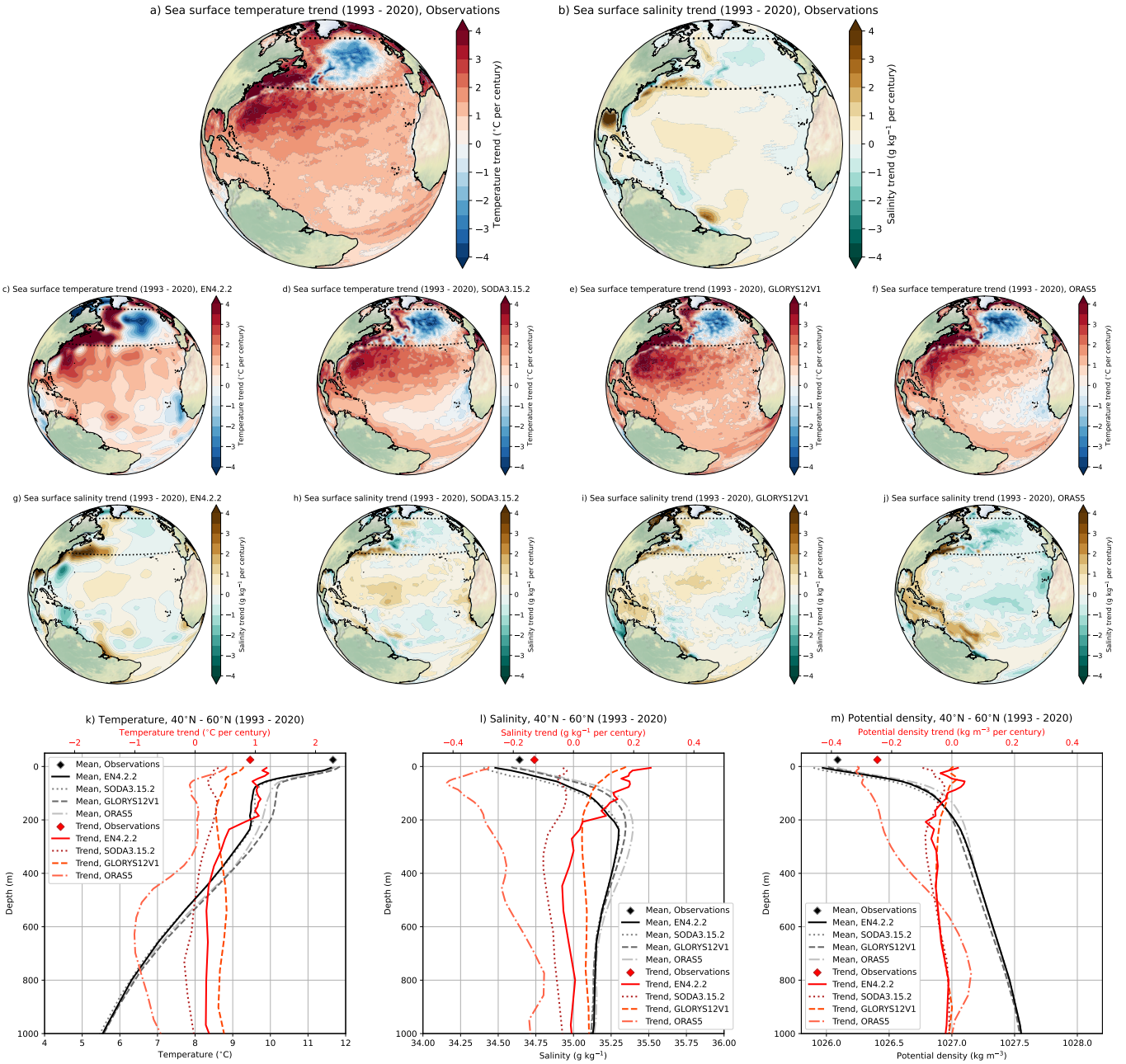


Fig. S7 Present-day oceanic climate change (1993 – 2020). (a – j): The sea surface temperature and sea surface salinity trends (1993 – 2020) for satellite observations, EN4.2.2, SODA3.15.2, GLORYS12V1 and ORAS5. (k – m): The vertical structure of temperature, salinity and potential density between 40°N – 60°N (Atlantic Ocean, dotted lines in panels a – j) and for the period 1993 – 2020. The black (red) curves are the time means (trends) for 1993 – 2020 and are shown for the different products. The diamond markers indicate the satellite observations.

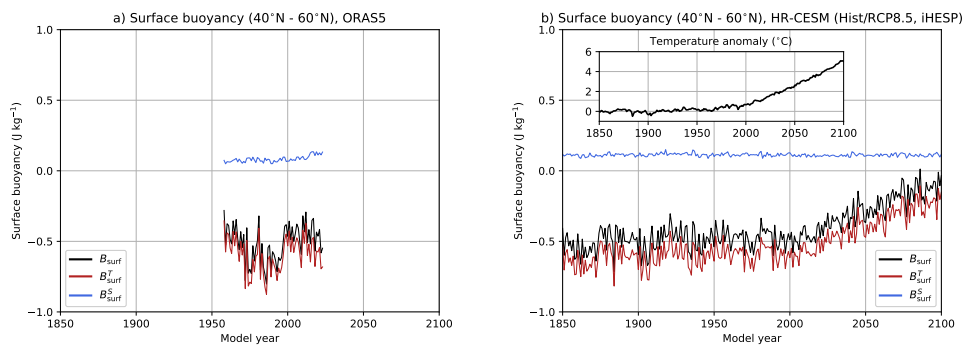


Fig. S8 Surface buoyancy changes under climate change. The surface buoyancy (B_{surf}) decomposition for (a): ORAS5 and (b): the high-resolution version of the CESM (iHESP) under the Hist/RCP8.5 scenario. The inset in panel b shows yearly-averaged global mean surface temperature anomaly compared to the historical period (1850 – 1899).

| Model name | Historical (1850 – 1899) | | | B_{surf} sign change | | | | Global warming of +3°C | | | | Average ΔB_{surf} (2000 – 2100) | |
|------------------|-----------------------------|------------------|------|-------------------------------|--------------|----------|--------------|------------------------|-------------------|----------|-------------------|---|-------------|
| | B_{surf} | F_{ovs} | AMOC | SSP2-4.5 | | SSP5-8.5 | | SSP2-4.5 | | SSP5-8.5 | | SSP2-4.5 | SSP5-8.5 |
| | | | | Year | ΔT_g | Year | ΔT_g | Year | B_{surf} | Year | B_{surf} | | |
| NESM3 | 0.151 | -0.17 | 6.8 | 1855 | 0.0 | 1855 | 0.0 | n.a. | n.a. | 2055 | 0.31 | 0.18 | 0.21 |
| IPSL-CM6A-LR | 0.111 | -0.17 | 10.2 | 1855 | 0.04 | 1855 | 0.04 | 2065 | 0.23 | 2051 | 0.18 | 0.12 | 0.17 |
| UKESM1-0-LL | 0.053 | 0.02 | 12.9 | 1855 | 0.04 | 1855 | 0.04 | 2058 | 0.26 | 2047 | 0.22 | 0.31 | 0.38 |
| CNRM-CM6-1-HR | 0.021 | -0.18 | 12.2 | 1855 | 0.02 | 1855 | 0.02 | 2063 | 0.19 | 2051 | 0.17 | 0.28 | 0.39 |
| CanESM5 | 0.017 | -0.08 | 10.1 | 1855 | -0.05 | 1855 | -0.05 | 2051 | 0.14 | 2041 | 0.14 | 0.12 | 0.29 |
| MRI-ESM2-0 | -0.015 | -0.24 | 15.3 | 1886 | -0.04 | 1886 | -0.04 | n.a. | n.a. | 2064 | 0.34 | 0.47 | 0.58 |
| CNRM-CM6-1 | -0.032 | -0.1 | 14.6 | 1909 | -0.24 | 1909 | -0.24 | 2085 | 0.26 | 2059 | 0.19 | 0.32 | 0.42 |
| MIROC6 | -0.056 | -0.08 | 13.9 | 1927 | 0.11 | 1927 | 0.11 | n.a. | n.a. | 2076 | 0.28 | 0.27 | 0.35 |
| CNRM-ESM2-1 | -0.071 | -0.11 | 15.6 | 1895 | -0.12 | 1895 | -0.12 | 2089 | 0.26 | 2064 | 0.2 | 0.35 | 0.44 |
| CMCC-CM2-SR5 | -0.115 | -0.08 | 18.1 | 2026 | 1.54 | 2017 | 1.41 | 2066 | 0.1 | 2052 | 0.07 | 0.19 | 0.3 |
| CMCC-ESM2 | -0.122 | -0.08 | 17.7 | 2012 | 1.21 | 2011 | 1.19 | 2066 | 0.04 | 2055 | 0.12 | 0.14 | 0.28 |
| MPI-ESM1-2-HR | -0.13 | -0.07 | 14.5 | 2015 | 1.08 | 2023 | 1.25 | n.a. | n.a. | 2074 | 0.15 | 0.19 | 0.26 |
| EC-Earth3-Veg | -0.139 | -0.02 | 12.3 | 2058 | 2.79 | 2055 | 3.32 | 2068 | 0.05 | 2050 | -0.04 | 0.23 | 0.36 |
| EC-Earth3-Veg-LR | -0.146 | -0.0 | 13.5 | 2055 | 2.17 | 2052 | 2.47 | 2089 | 0.05 | 2062 | 0.09 | 0.19 | 0.33 |
| MPI-ESM1-2-LR | -0.18 | 0.11 | 17.5 | 2014 | 1.0 | 2013 | 1.02 | n.a. | n.a. | 2071 | 0.1 | 0.2 | 0.23 |
| EC-Earth3-CC | -0.193 | 0.01 | 12.9 | 2066 | 2.78 | 2047 | 2.5 | 2072 | -0.03 | 2057 | 0.06 | 0.19 | 0.35 |
| EC-Earth3 | -0.211 | -0.03 | 14.7 | 2066 | 2.66 | 2065 | 3.44 | 2088 | 0.03 | 2058 | -0.02 | 0.24 | 0.34 |
| GFDL-CM4 | -0.228 | 0.03 | 16.8 | 2053 | 2.12 | 2044 | 2.12 | 2093 | 0.07 | 2060 | 0.06 | 0.28 | 0.45 |
| ACCESS-CM2 | -0.249 | 0.06 | 16.9 | n.a. | n.a. | 2072 | 4.12 | 2070 | -0.03 | 2056 | -0.07 | 0.2 | 0.41 |
| FGOALS-F3-L | -0.279 | 0.44 | 14.3 | n.a. | n.a. | n.a. | n.a. | n.a. | n.a. | 2060 | -0.21 | 0.17 | 0.21 |
| ACCESS-ESM1-5 | -0.34 | 0.1 | 16.2 | n.a. | n.a. | n.a. | n.a. | 2090 | -0.18 | 2061 | -0.16 | 0.21 | 0.28 |
| NorESM2-MM | -0.38 | 0.17 | 22.0 | n.a. | n.a. | 2067 | 2.5 | n.a. | n.a. | 2077 | 0.03 | 0.39 | 0.63 |
| NorESM2-LM | -0.383 | 0.2 | 21.1 | 2083 | 2.0 | 2061 | 2.21 | n.a. | n.a. | 2078 | 0.13 | 0.49 | 0.76 |
| FGOALS-g3 | -0.468 | 0.36 | 24.3 | n.a. | n.a. | n.a. | n.a. | n.a. | n.a. | 2073 | -0.15 | 0.23 | 0.46 |
| CMIP6 mean | -0.141 | 0.0 | 15.2 | 2043 | 1.96 | 2036 | 1.88 | 2087 | 0.09 | 2059 | 0.08 | 0.25 | 0.37 |

Table S1 Overview of the CMIP6 models, ranked on their historical (1850 – 1899) surface buoyancy (B_{surf} , in J kg^{-1}) value, including their historical freshwater transport at 34°S (F_{ovs} , in Sv) and AMOC strength at 1,000 m and 26°N (in Sv). For each CMIP6 model, we determined the first 11-year window (e.g., 2055 → 2050 – 2060) where B_{surf} switches sign and the associated global mean surface temperature anomaly (ΔT_g , in °C) compared to the historical period. Similarly, the first 11-year window where the global surface temperature anomaly exceeds 3°C warming and the associated B_{surf} value. The last two columns display the average B_{surf} change (i.e., linear trend) over the 21st century, where bold indicates significant ($p < 0.05$, [35]) changes. For the CMIP6 mean, we first determined the multi-model mean and then determined the presented quantities.